

Coherent switching by detuning a side-coupled quantum-dot system

Omar Valsson,^{1,*} Chi-Shung Tang,^{2,†} and Vidar Gudmundsson^{1,‡}

¹*Science Institute, University of Iceland, Dunhaga 3, IS-107 Reykjavik, Iceland*

²*Department of Mechanical Engineering, National United University, 1, Lienda, Miaoli 36003, Taiwan*

We investigate phase coherent electronic transport in an open quantum system, which consists of quantum dots side-coupled to a nanowire. It is demonstrated that coherent switching can be characterized by adjusting the electronic energy. A comparative analysis of quantum coherence effects in side-coupled quantum-dot systems is presented. Our results demonstrate the relevance of electronic nanodevices based on coherent switching by appropriately detuning the side-coupled quantum dots that are located at variable distance along a wire.

PACS numbers: 73.23.-b, 73.21.Hb, 73.21.La, 85.35.Ds

I. INTRODUCTION

Transport through mesoscopic systems has received enormous interest within the last decade.^{1,2} The advances in current progress in microfabrication technology have enabled studies of transport through quantum systems in which the charge carriers behave coherently. In recent years, much effort has been devoted to coherent transport in various coupled quantum-dot and quantum-wire associated structures such as open quantum dot,^{3,4,5,6,7} embedded dot,^{8,9,10} side-coupled-dot,^{11,12,13,14,15} antidot,^{16,17,18} multidot,^{19,20} and coupled quantum-wire systems.^{21,22,23} Rich quantum interference phenomena in mesoscopic systems have been discussed in various aspects such as bound-state features,^{24,25,26,27,28} spin-related switching,^{29,30,31} phase switching,^{32,33} and Andreev current switching.³⁴ Over the last few years, the search for the quantum transport through quantum-dot systems has made great progress. For example, coherent probing experiment for investigating phase switching of Aharonov-Bohm oscillation in differential conductance in a two-dot embedded quantum ring has been performed.³² The study of switching effects has thus drawn a great deal of interest in application and at the fundamental level.

Theoretically, transport investigations in quantum-dot systems are often based on the Anderson model.³⁵ Commonly, it has been assumed that the geometry is discrete in real space and the coupling between the system and the external electrodes is relatively weak.^{36,37,38} The open systems considered were usually idealized to be strictly one-dimensional implying the assumption of a single-mode propagation, namely that the finite width effect of the system was not included. Alternatively, the Lippmann-Schwinger formalism assumes a continuous model that has been used to calculate the electronic and atomic dynamics of nanoscale conductors under steady-state current flow.^{39,40} This theory was subsequently applied considering electronic transport through laterally parallel double open quantum dots embedded inside a quantum wire.⁷ It allowed us to look at arbitrary multidot potential profiles and illustrate the results by performing computational simulations for the electronic

conductance through the system with multi-mode propagation. We found that the coupling modes of the dots are tunable by adjusting the strength of a central barrier in the wire.

In this present work, we utilize the Lippmann-Schwinger formalism to achieve a full quantum mechanical description of the dynamics of side-coupled quantum-dot systems. We solve a set of coupled Lippmann-Schwinger equations to express each individual continuum wave function of the entire system in terms of the corresponding asymptotic wave function of the source-drain leads, and the scattering potential representing the mesoscopic system via the appropriate scattering Green function. Transport regimes arising from the strong interplay between the dot structures and the open mesoscopic system are investigated.

The paper is organized as follows. In Sec. II we present the general scheme and description of quantum transport calculation based on the framework of Lippmann-Schwinger formalism. In Sec. III, the manipulation of the side-coupled quantum dots is addressed. Coherent switching effects by either tuning the electronic energy or detuning one of the side-coupled dots are discussed. Finally, in Sec. IV we shall summarize and draw conclusions.

II. LIPPMANN-SCHWINGER MODEL

The physical system under investigation is a two-dimensional nanowire with side-coupled quantum dots. The considered infinitely long wire allows electrons to propagate along the wire direction while being confined transversely. The considered mesoscopic system can be viewed as three divided regions, namely the left source lead, the scattering region including the side-coupled dots, and the right drain lead, as is depicted in Fig. 1. The Hamiltonian describing the system can be written as

$$H = H_0 + V_{sc}(x, y), \quad (1)$$

where V_{sc} is the scattering potential describing the side-coupled quantum dots, localized inside the scattering re-

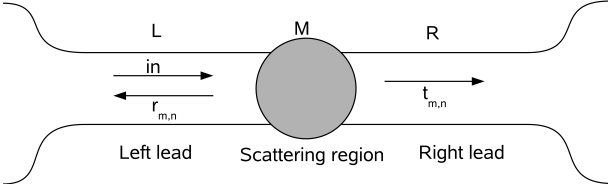


FIG. 1: Schematic diagram of a scattering region in a nanowire connected to electronic reservoirs.

gion. The unperturbed Hamiltonian is given by

$$H_0 = -\frac{\hbar^2}{2m^*}\nabla^2 + V_c(y), \quad (2)$$

where m^* stands for the effective mass of the electron. The confining potential $V_c(y)$ is assumed of the parabolic form

$$V_c(y) = \frac{1}{2}m^*\omega^2 y^2, \quad (3)$$

leading to the discrete subband energy levels

$$\varepsilon_n = \left(n + \frac{1}{2}\right)\hbar\omega, \quad (4)$$

with $n = 0, 1, 2, \dots$ and level spacing $\Delta\varepsilon_n = \hbar\omega$.

For the n -th mode and without magnetic field, the unperturbed eigenfunctions of H_0 can be expressed as $\exp[\pm ik_n x]\chi_n(y)$, where $\chi_n(y)$ stands for the confinement modes of the nanowire, determined by

$$\left[-\frac{\hbar}{2m^*}\frac{d^2}{dy^2} + V_c(y)\right]\chi_n(y) = \varepsilon_n\chi_n(y), \quad (5)$$

and the wave number k_n is given by

$$k_n = \sqrt{\frac{2m^*}{\hbar^2}(E - \varepsilon_n)}. \quad (6)$$

We would like to mention that the real wave number k_n implies the n -th mode being a propagating mode, otherwise it indicates an evanescent mode that plays an important role to quantum interference in coherent transport. For an electron incident from the source electrode with energy E occupying the mode n , the electron may be reflected into mode m with amplitude $r_{m,n}$ or transmitted into mode m with amplitude $t_{m,n}$ to the drain electrode. The corresponding wave function describing the scattering processes can be expressed as

$$\Psi_{E,n}(x,y) = \exp(ik_n x)\chi_n(y) + \sum_m r_{m,n}\exp(-ik_m x)\chi_m(y), \quad (7)$$

if $(x,y) \in L$;

$$\Psi_{E,n}(x,y) = \sum_m \varphi_{E,n;m}(x)\chi_m(y), \quad (8)$$

if $(x,y) \in M$; and

$$\Psi_{E,n}(x,y) = \sum_m t_{m,n}\exp(ik_m x)\chi_m(y), \quad (9)$$

if $(x,y) \in R$. Here L , M , and R denote the left source lead, the scattering region, and the right drain lead, respectively. In addition, $\varphi_{E,n;m}(x)$ represents the x component of the m -th mode scattering wave function in the scattering region. This allows us to expand the Schrödinger equation in the scattering region into a set of coupled differential equations

$$\left(\frac{d^2}{dx^2} + k_m^2\right)\varphi_{E,n;m}(x) = \frac{2m^*}{\hbar^2}\sum_{m'} V_{m,m'}(x)\varphi_{E,n;m'}(x), \quad (10)$$

in which all evanescent and propagating intermediate modes m' are taken into account. The coupling between these intermediate modes is characterized by the matrix elements of the scattering potential, namely

$$V_{m,m'}(x) = \int dy \chi_m^*(y)V_{sc}(x,y)\chi_{m'}(y), \quad (11)$$

Here, the matrix elements are calculated analytically.

To obtain the Lippmann-Schwinger equation for handling the transport properties, we start from the unperturbed Green function, that obeys the differential equation

$$\left(\frac{d^2}{dx^2} + k_m^2\right)G_{E,m}^0(x,x') = \delta(x-x'), \quad (12)$$

describing the electron incident from the source electrode. This unperturbed Green function can be expressed as

$$G_{E,m}^0(x,x') = \frac{1}{2ik_m}\exp(ik_m|x-x'|), \quad (13)$$

and is utilized to transform from the differential equations (10) into an infinite set of coupled Lippmann-Schwinger equations

$$\varphi_{E,n;m}(x) = \delta_{n,m} \exp(ik_m x) + \frac{2m^*}{\hbar^2} \sum_{m'} \int dx' G_{E,m}^0(x, x') V_{m,m'}(x') \varphi_{E,n;m'}(x'). \quad (14)$$

The transmission amplitude $t_{m,n}$ for transmission from the n -th mode to the m -th mode can be found by looking at the asymptotic limit $x \gg 0$, resulting in

$$t_{m,n}(E) = \delta_{m,n} + \frac{m^*}{i\hbar^2 k_m} \sum_{m'} \int dx' \exp(-ik_m x') V_{m,m'}(x') \varphi_{E,n;m'}(x'), \quad (15)$$

where m and n are propagating modes.

Based on the framework of the well known Landauer-Büttiker formalism,^{41,42} the transmission probability

$$T_{m,n} = \frac{k_m}{k_n} |t_{m,n}(E)|^2 \quad (16)$$

can be calculated numerically at the Fermi surface, and the conductance is related to the transmission,⁴³ expressed as

$$G(E) = \frac{2e^2}{h} \sum_{n,m} T_{m,n}(E), \quad (17)$$

where the sum is over all propagating modes.

It is worth mentioning that the solution of the coupled Lippmann-Schwinger equations (14) is achieved by putting the x variable on a grid. The integrals are computed by using extended Bode's rule⁴⁴ for numerical integration, taking care of the cusp in the Green function (13) at $x = x'$ before integrating.

Finally, we note that the above Lippmann-Schwinger model is quite general towards the choice of a confinement and scattering potentials.

III. RESULTS AND DISCUSSION

To explore the electronic transport properties in an open mesoscopic system consisting of a nanowire influenced by side-coupled quantum dots, we assume the system to be fabricated in a high-mobility GaAs-Al_xGa_{1-x}As heterostructure forming a two-dimensional electron gas such that the effective mass of an electron is $m^* = 0.067 m_0$ with m_0 being the free electron mass. In addition, we select the confinement parameter such that the energy level spacing is $\Delta\varepsilon_n = \hbar\omega = 1$ meV. In the numerical calculation, it is convenient to redefine the energy scale by the lowest subband energy $\varepsilon_0 = \hbar\omega/2 = 0.5$ meV and the length scale by the characteristic length $a_\omega = \sqrt{m^*\omega/\hbar} = 33.7$ nm. In all the figures shown below, we have defined the energy-related parameter

$$X_E = \frac{E}{2\varepsilon_0} + \frac{1}{2}, \quad (18)$$

where the integral part of X_E indicates the number of propagating modes at the energy E .²⁴ We note that numerical accuracy was always carefully checked and the calculations were performed using in total 20 subbands and 301 grid points. In the following, we shall investigate the dynamic motion of the electronic wave in a quantum wire with side-coupled quantum dots.

A. Single and double side-coupled quantum dot systems

A side-coupled quantum dot system can be regarded as an open mesoscopic system with transport characteristics that are tunable by a kind of side-stub nanostructures. In contrast to the embedded quantum-dot system, the transmission through the side-coupled quantum-dot system consists of a quantum interference between the ballistic nanowire and the resonant channels in the side-coupled nanostructures. Recent works dealing with side-coupled quantum-dot system rely mainly on an Anderson model in which the side-coupled dots are assumed to behave effectively like artificial quantum impurities.^{45,46} It is thus warranted to devote further effort in developing numerical techniques in order to analyze the quantum behavior of the electronic transport in a side-coupled quantum-dot system with an expected smooth profile.

We start by modeling a quantum wire with single or double side-coupled quantum dots, placed symmetrically in parallel on each side of the nanowire. The scattering potential describing the pair of quantum dots is modeled by a linear combination of four Gaussian functions

$$V_{sc}(x, y) = V_{1a} e^{-[\beta_{x,1a}(x-x_1)^2 + \beta_{y,1a}(y-y_1)^2]} + V_{1b} e^{-[\beta_{x,1b}(x-x_1)^2 + \beta_{y,1b}(y-y_1)^2]} + V_{2a} e^{-[\beta_{x,2a}(x-x_2)^2 + \beta_{y,2a}(y-y_2)^2]} + V_{2b} e^{-[\beta_{x,2b}(x-x_2)^2 + \beta_{y,2b}(y-y_2)^2]}, \quad (19)$$

where the first two terms describe the geometry of quantum dot 1 and the last two terms are associated to quantum dot 2, as is depicted in Fig. 2(a). In this subsection, we focus on two identical side-coupled dots, namely with $V_{1a} = V_{2a} = -36$ and $V_{1b} = V_{2b} = 20$ in units of ε_0 . In addition, we assume that the two quantum dots are

in parallel and at the same distance on opposite sides of the nanowire, centered at $(x_1, y_1) = (6, 4)$ and $(x_2, y_2) = (6, -4)$ in units of a_ω , respectively. Moreover, the form factors describing the broadening of the quantum dots are selected as $\beta_{x,1a} = \beta_{y,1a} = \beta_{x,2a} = \beta_{y,2a} = 0.4$ and $\beta_{x,1b} = \beta_{y,1b} = \beta_{x,2b} = \beta_{y,2b} = 0.2$ in units of a_ω^{-2} , respectively. In Fig. 2(b), we show the transverse profiles due to the contributions of the confining and the scattering potentials at $x = x_1$. The dashed-green curve indicates the transverse potential profile of the unperturbed nanowire, and the double side-coupled dot system has a potential profile illustrated by the solid-red curve. Later on, we shall adjust the parameter V_{2a} of the lower quantum dot 2 by ΔV_{2a} , thus varying the depth of dot 2, for studying the sensitivity and dynamics of quantum interference effects.

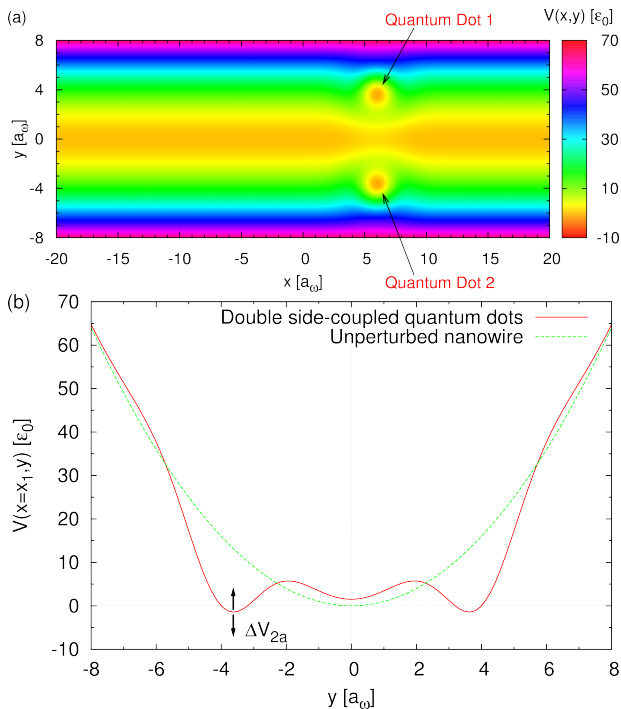


FIG. 2: (Color online) Diagram of the system under investigation. (a) Double quantum dots side-coupled to a nanowire. (b) Transverse potential profile at $x = x_1$ for the double quantum dots side-coupled to a nanowire (solid red) in comparison with the unperturbed nanowire (dashed green).

In Fig. 3 we show the conductance as a function of the parameter X_E for the lowest two conductance plateaus for the case of double side-coupled dots (solid red) in comparison with the case of a single side-coupled dot (dashed blue) and the unperturbed nanowire (dotted green). In the absence of a side-coupled quantum dots, the conductance of the ideal nanowire reproduces the well known conductance quantization plateaus in units of $G_0 = 2e^2/h$. For the case of a single side-coupled dot and the instate in the low kinetic energy regime, the conductance is strongly suppressed due to an enhanced backscattering by the quantum dot. The backscattering

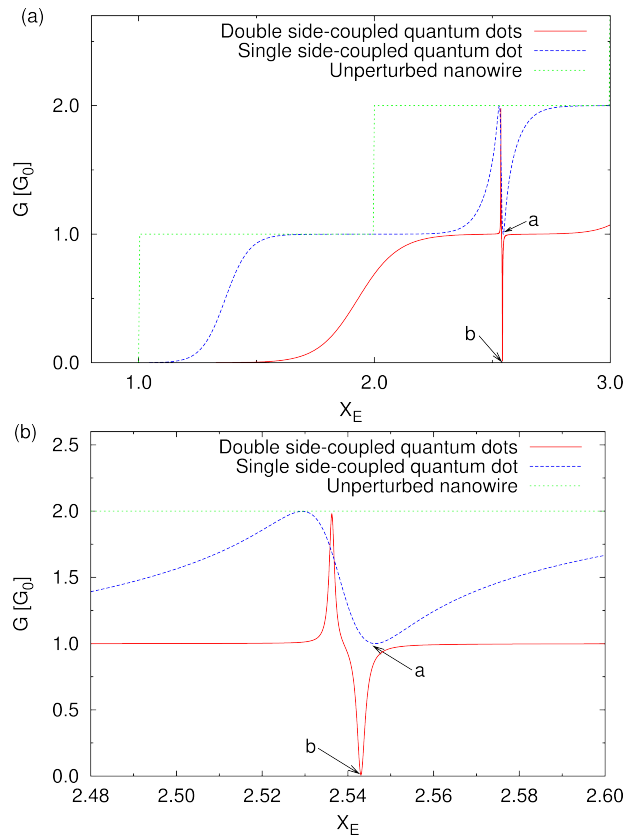


FIG. 3: (Color online) (a) Conductance as a function of the parameter X_E for the cases of double side-coupled quantum dots (solid red), single side-coupled quantum dot (dashed blue), and unperturbed nanowire (dotted green). The conductance curves exhibiting Fano resonances are emphasized in (b).

effect is blue shifted by including the second quantum dot. This interesting conductance suppression effect can be applied as a conductance switching at $X_E \approx 1.0$ by turning on and off the quantum dot 2 by tuning a gate voltage used to form it.

In the mediate kinetic energy regime of the second subband region, there is a clear antisymmetric peak-and-dip structure in the conductance around $X_E \approx 2.54$, exhibiting the well-known Fano resonance feature.⁴⁷ This is attributed to quantum interference between the continuum in the wire and the quasibound state in the side-coupled quantum dots. Both in the single and double side-coupled-dot systems, the Fano peaks can reach $2G_0$. However, the Fano dip of the single-dot case reaches G_0 but the Fano dip of the double-dot case may be suppressed to zero conductance. This implies that only the electrons occupying the second subband contribute to the resonance reflection for the case of single-dot, however for the case of double-dot the electrons occupying both subbands may contribute to the resonant reflection leading to the $2G_0$ drop from the Fano peak.

To demonstrate the above Fano resonance behavior in conductance we show, in Figs. 4 and 5, the square root

of the probability densities of the scattering states at the dip structures in Fig. 3 marked by **a** ($E = 4.0927 \varepsilon_0$) for the case of a single side-coupled dot and the dip marked by **b** ($E = 4.0861 \varepsilon_0$) for the case of double side-coupled dots, respectively. For the single-dot case, the electron occupying the first subband ($n=0$) are in an extended state with negligible coupling to the upper dot, however the electron occupying the second subband ($n=1$) couple strongly to the upper dot and are resonantly reflected. For the case of double side-coupled dots, both the electrons occupying the first and the second subbands are able to couple strongly to the side-coupled dots and are resonantly reflected. Consequently, for the cases of a single and double side-coupled quantum dots, the strengths of the Fano lineshapes are G_0 or $2G_0$, respectively. We would like to mention in passing that the scattering states for the peak and the dip are very similar, showing a strong and long-lived quasibound state feature that is localized in each of the two quantum dots. The shape of the quasibound states indicates that these are the lowest quasibound states in the quantum dots.

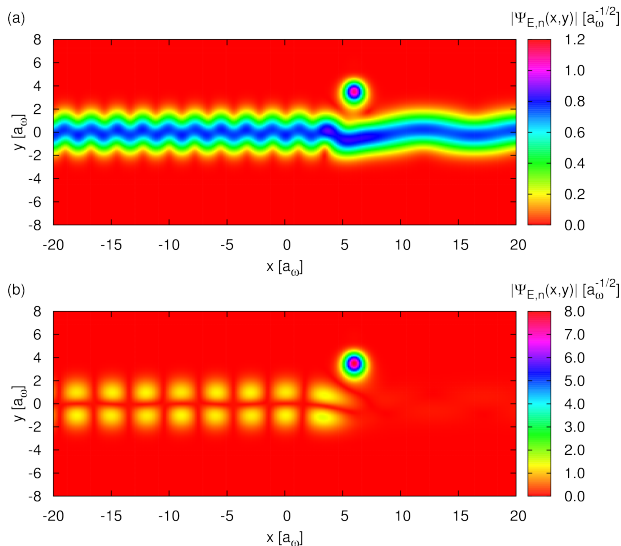


FIG. 4: (Color online) Square root of probability densities of the scattering states for the case of single-dot system corresponding to the Fano resonance dip marked by **a** in Fig. 3 for the electrons occupying the incident subband (a) $n=0$; and (b) $n=1$.

B. Detuning effects in a double side-coupled quantum dot system

Double quantum dot systems are good candidates for revealing coherent quantum transport properties. Energy detuning between the different quantum-dot levels can be experimentally investigated by using charging diagram measurements or using an excitation spectroscopy technique.⁴⁸ From application point of view, it was found that the conduction in a cavity mode with detuning pa-

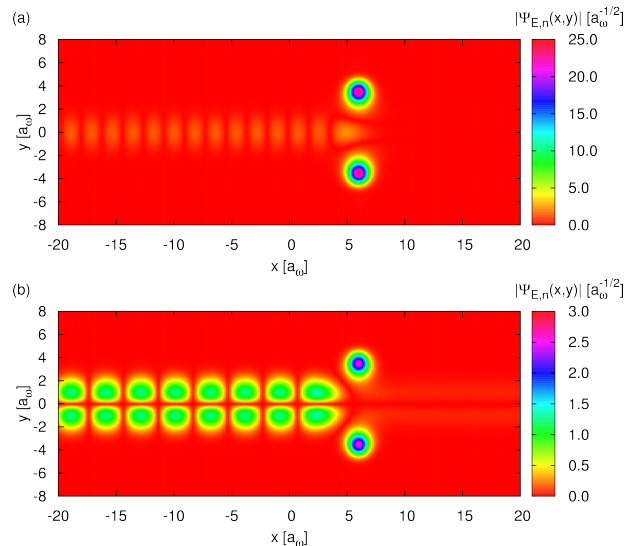


FIG. 5: (Color online) Square root of probability densities of the scattering states for the case of double-dot system corresponding to the Fano resonance dip marked by **b** in Fig. 3 for the electrons occupying the incident subband (a) $n=0$; and (b) $n=1$.

rameter may be utilized as a quantum bit readout.⁴⁹ It is thus warranted to investigate the detuning effects by considering a parallel side-coupled double-dot system.

The physical parameters considered here are the same as in the previous subsection such that the two side-coupled dots are identical and the system remains spatially symmetric. The lower quantum dot 2 is adjusted by the parameter ΔV_{2a} by tuning a gate voltage so that the energy levels of the lower quantum dot 2 are relatively detuned and the spatial symmetry of the system is broken. As a result, the symmetry of the quasibound state feature causing the Fano resonance (see Fig. 3) tends to be destroyed by increasing the detuning potential. Comparing to overall scattering potentials and characteristic energies, the detuning parameters are assumed to be relatively small such that the detuning only has an effect on the resonance structure around $X_E \approx 2.5$.

Figure 6 demonstrates the conductance as a function of the parameter X_E as well as the detuning parameter ΔV_{2a} . The deviation of the peak and the dip structures forming the Fano lineshape tends to be suppressed by increasing the detuning potential. Both the peak and the dip structures get less pronounced and the peak may crossover to a dip when the detuning parameter ΔV_{2a} is sufficiently large. Also, we observe an avoided crossing of the peak and the dip during variation of the detuning parameter through zero.

In Fig. 7, we present the conductance characteristics with detuning parameter $\Delta V_{2a} = -0.14 \varepsilon_0$ (solid red) in comparison to the case without detuning $\Delta V_{2a} = 0.0 \varepsilon_0$ (dashed blue). Furthermore, in Figs. 8, 9, and 10, we present, in order of energy, the square root of the probability densities of the scattering states at the energies

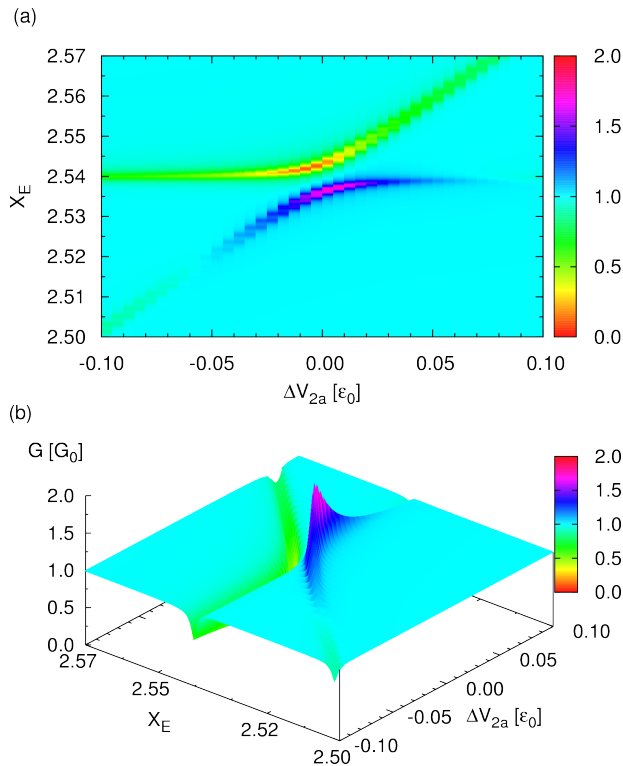


FIG. 6: (Color online) Conductance as functions of the parameter X_E and detuning parameter ΔV_{2a} for the case of double side-coupled quantum dots: (a) Top view; (b) 3D view.

labeled by **e**, **f**, and **g**, respectively, in Fig. 7. In the presence of detuning $\Delta V_{2a} = -0.14 \epsilon_0$, two significant Breit-Wigner dips are found at $E = 3.9725 \epsilon_0$ (labeled by **e**) and $4.0798 \epsilon_0$ (labeled by **g**). It turns out that the anti-resonant dip features are significantly different from the antisymmetric Fano resonance for the symmetric case in the absence of detuning. It is worth mentioning that these Breit-Wigner structures in conductance are associated to the long-lived quasibound states in the lower dot for case **e** and in the upper dot in for case **g**, as illustrated in Fig. 8 and Fig. 10 respectively. This important feature demonstrates the possibility of *coherent switching* between the lower and the upper side-coupled dots by appropriately adjusting the electronic energy. This could have interesting applications in quantum interference devices based on coherent control of the quantum interference of side-coupled double quantum dots.

We would like to bring attention in passing that the real space probability density of the scattering states shown in Fig. 9 corresponding to the point **f** of solid red curve in Fig. 7 has significant coupling between the extended propagating modes in the quantum channel and both the side-coupled quantum dots. In addition, the quasibound states localized in each quantum dots are considerably suppressed and the scattering behavior is much weaker than both the cases **e** and **g**.

The peak-to-dip crossover feature demonstrated in Fig. 6 motivates us to investigate further the processes around

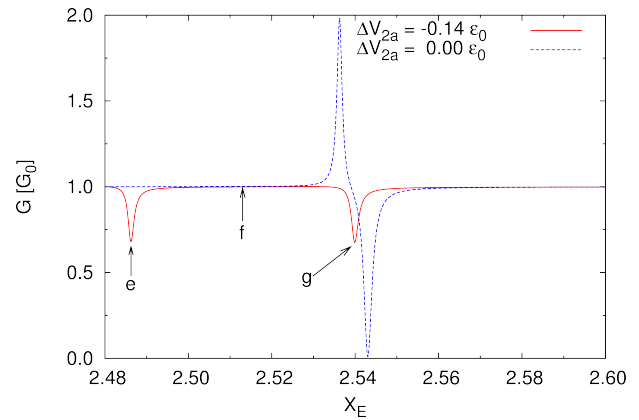


FIG. 7: (Color online) Conductance as a function of the parameter X_E of the double side-coupled quantum dots for the cases with detuning $\Delta V_{2a} = -0.14 \epsilon_0$ (solid red) and with no detuning $\Delta V_{2a} = 0.0 \epsilon_0$ (dashed blue).

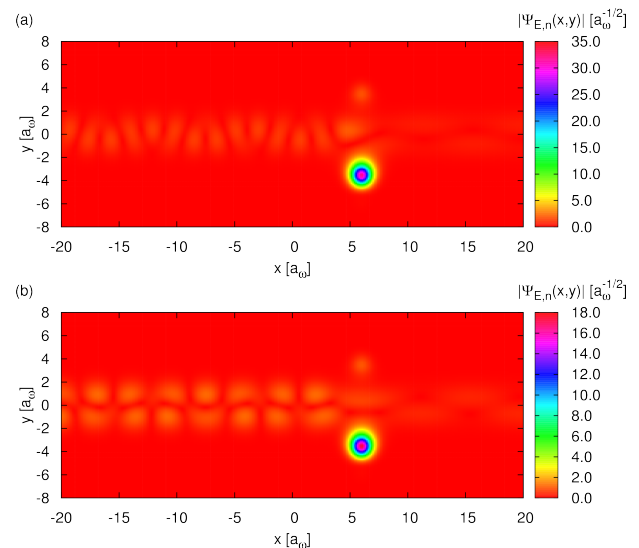


FIG. 8: (Color online) Square root of probability densities of the scattering states at the dip structure in conductance marked by **e** in Fig. 7 for the case of $\Delta V_{2a} = -0.14 \epsilon_0$ with incident subband (a) $n=0$; and (b) $n=1$.

$\Delta V_{2a} \approx -0.05 \epsilon_0$ where only a single peak is significantly visible. In Fig. 11(a), we thus focus on the conductance as a function of the rescaled electron energy for the case of $\Delta V_{2a} = -0.055 \epsilon_0$ that is presented by solid red curve in comparison with the case with no detuning shown by dashed blue curve. First, we find a small blip marked by **j** ($E = 4.0365 \epsilon_0$). A zoom-in figure for clearly demonstrating the blip structure is illustrated in Fig. 11(b) in comparison with the cases of $\Delta V_{2a} = -0.050 \epsilon_0$ (dash-dotted brown) and $-0.060 \epsilon_0$ (dotted green) for showing the sensitivity nature of the blip structure in conductance. To understand better the transport mechanism of the blip structure marked by **j**, it is helpful to compare with the square root probability density in the real space

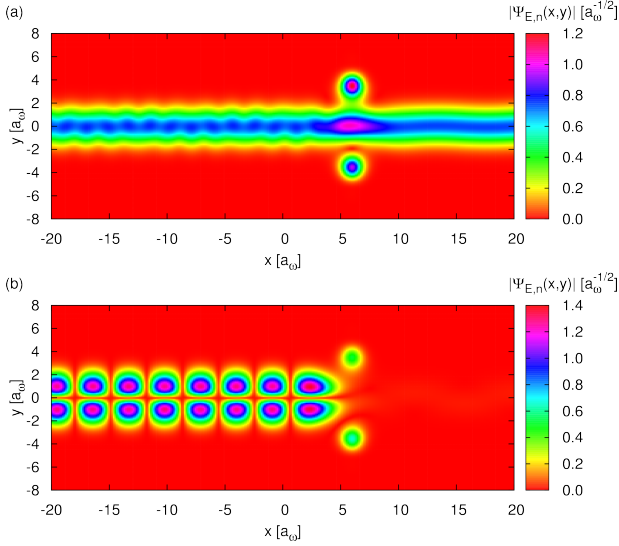


FIG. 9: (Color online) Square root of the probability densities of the scattering states marked by \mathbf{f} in Fig. 7 for the case of $\Delta V_{2a} = -0.14 \epsilon_0$ with incident subband (a) $n=0$; and (b) $n=1$.

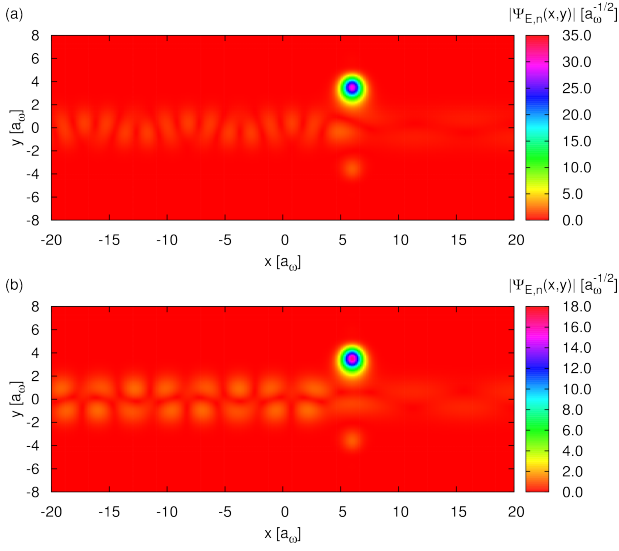


FIG. 10: (Color online) Square root of the probability densities of the scattering states at the dip structure in conductance marked by \mathbf{g} in Fig. 7 for the case of $\Delta V_{2a} = -0.14 \epsilon_0$ with incident subband (a) $n=0$; and (b) $n=1$.

shown in Fig. 12. Electrons entering the system in the lowest two subbands mainly form long-lived quasibound states in the lower side-coupled quantum dot 1. Second, we would like to see the point marked by \mathbf{k} that is an energy regime between the blip structure \mathbf{j} and the dip structure \mathbf{l} . The localized electrons tend to be coupled to the central quantum channel as shown in Fig. 13. The $n=0$ mode exhibits stronger coupling to the upper dot and manifests a high transmission feature, however the $n=1$ mode with higher coupling to the lower dot exhibits

a total reflection.

Concerning the point marked by \mathbf{l} ($E = 4.0804 \epsilon_0$), the electrons occupying the lowest two subbands tend to form long-lived quasibound states in the upper dot. These interesting features accessible by adjusting the electronic energy from \mathbf{j} to \mathbf{l} may be applicable for *coherent switching* of charge accumulation between the lower and the upper dot. We note that the small blip marked by \mathbf{j} can induce a strong and long-lived bound state in quantum dot 2. This is not straight forward expected from the relationship of lifetime and full-width at half-maximum of the resonance structures in the conductance. This counterintuitive feature in conductance is related to an occurrence of a bound state in continuum (BIC) in the double side-coupled quantum dot system.

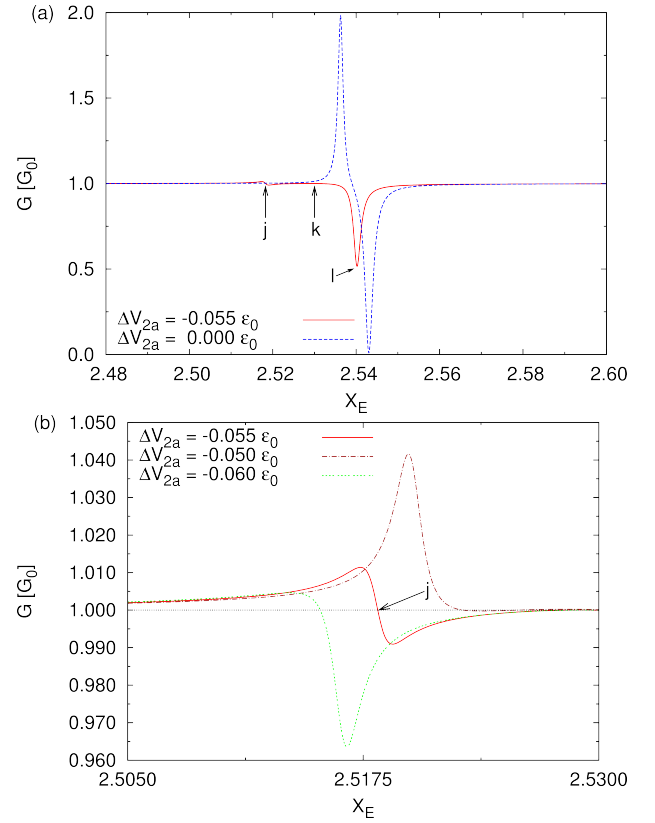


FIG. 11: (Color online) (a) Conductance as a function of the parameter X_E in a nanowire with double side-coupled quantum dots for the cases with detuning $\Delta V_{2a} = -0.055 \epsilon_0$ (solid red) and with no detuning $\Delta V_{2a} = 0.0 \epsilon_0$ (dashed blue). The small blip structure marked by \mathbf{j} in (a) is emphasized in (b)

BIC is a discrete energy normalizable bound state above the continuum threshold in energy, having vanishing resonance width and in principle infinite lifetime. Shortly after that the Schrödinger equation was put forward were von Neumann and Wigner the first to predict the existence of the BIC phenomenon.⁵⁰ There, the BIC behavior was regarded as a mathematical curiosity attributed to rather unphysical spherically symmetric po-

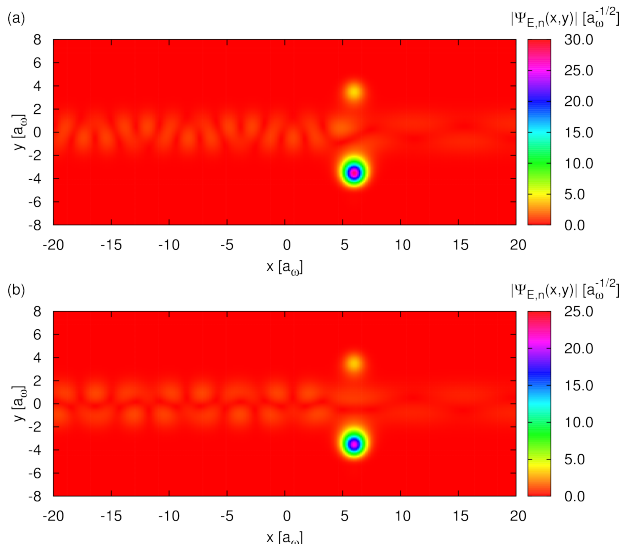


FIG. 12: (Color online) Square root of the probability densities of the scattering states at the small blip in conductance marked by \mathbf{j} in Fig. 11 with detuning parameter $\Delta V_{2a} = -0.055 \varepsilon_0$ for the cases of incident subband (a) $n=0$; and (b) $n=1$.

tentials. Later on, more detailed analysis of the BIC was presented by Stillinger and Herrick.⁵¹ Friedrich and Wintegen showed that the BIC may occur due to the interference of resonances that can be analyzed using the Feshbach resonance theory:⁵² Suppose two resonances can be tuned as a function of a continuous parameter, for a certain condition one of the resonances may have a vanishing resonant width. This fact was discussed in a number of physical systems both with analytical and numerical models.^{27,53,54,55} It is worth mentioning that the resonance width can also turn to zero in open systems such as the angle of a bent waveguide is varied.⁵⁶ The BIC has also been discussed in the context of nuclear dynamics on coupled potential surfaces.⁵⁷ Furthermore, it has also been proposed that the BIC causes a very narrow absorption peak in a semiconductor heterostructure superlattice.⁵⁸

In our system, the two resonant states are the quasibound states in the two side-coupled quantum dots and the continuous parameter is the detuning parameter ΔV_{2a} . However, it has not been reported that a BIC structure in conductance can be controlled by appropriately detuning one of a side-coupled quantum dots. Furthermore, we would like to bring attention to that the strong quasibound state at the blip structure in the conductance is not the BIC but an indication of the existence of such a state in the double side-coupled quantum dot system, since the BIC or the “ghost Fano resonance” feature has been predicted to occur only when the configuration is totally symmetric.⁵⁴

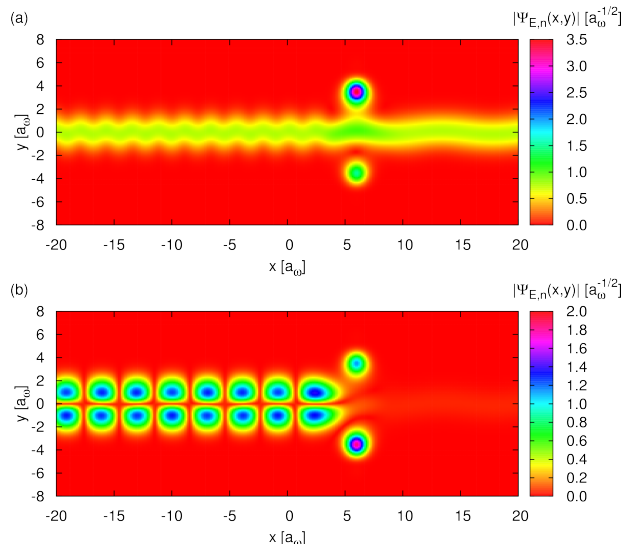


FIG. 13: (Color online) Square root of the probability densities of the scattering states marked by \mathbf{k} in Fig. 11 with detuning parameter $\Delta V_{2a} = -0.055 \varepsilon_0$ for the cases of incident subband (a) $n=0$; and (b) $n=1$.

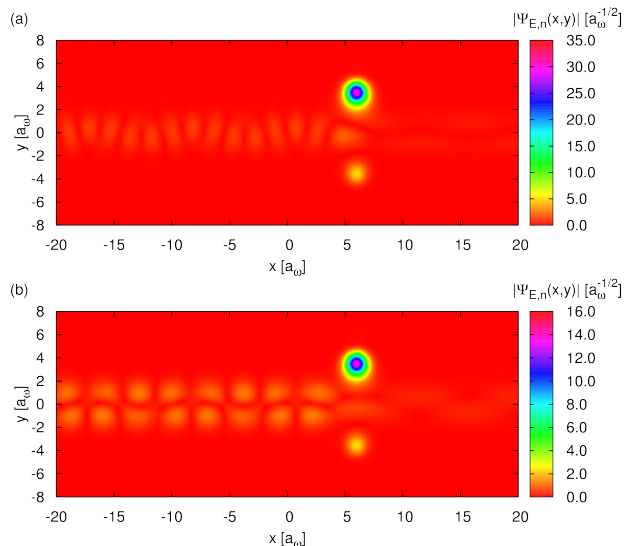


FIG. 14: (Color online) Square root of the probability densities of the scattering states at the dip marked by \mathbf{l} in Fig. 11 with detuning parameter $\Delta V_{2a} = -0.055 \varepsilon_0$ for the cases of incident subband (a) $n=0$; (b) $n=1$.

IV. CONCLUDING REMARKS

We have developed a theoretical model by implementing the Lippmann-Schwinger formalism to demonstrate and elucidate the quantum transport properties of a quantum dot systems side-coupled to a nanowire. In the present work, we propose that the conductance can be switched on and off by turning on and off one of the side-coupled double quantum dots controlled by using a gate voltage. It has been verified experimentally that a

conductance switching can be achieved either in a conducting polymer wire by controlling the redox state of the polymer with a potential of the nanoelectrodes.⁵⁹ Theoretically, Taylor and co-workers also investigated the conductance switching features in a molecular device for studying the effect of side groups on the electrical properties of a monolayer.⁶⁰

Furthermore, we have demonstrated the possibility of using the detuning parameter to achieve *coherent switching* between the lower and the upper side-coupled dots by appropriately adjusting the electronic energy. This may be utilized in designing quantum devices based on the coherent control of the side-coupled dots. For the case of slight detuning, say $\Delta V_{2a} = -0.055$, we have found a small blip structure in conductance that is very sensitive to the detuning parameter. Coherent switching of charge accumulation for this case is proposed and its relation to the BIC feature is also discussed. Similar coherent switching features can be found in the case of quadrupole side-coupled quantum-dot system by means of detuning technique, but the analysis is more difficult due to the complicated quantum interference among the

four dots. The significantly different conductance properties, however, will be discussed elsewhere. In order to reveal the coherence switching and the dynamics of electronic transport in a side-coupled quantum-dot system, more intricate measurements are required. We wish that the above proposed switching effects will stimulate experimental efforts in the near future.

Acknowledgments

The authors acknowledge financial support from the Icelandic Research Fund for Graduate Students, the Icelandic Research Fund, the Research Fund of the University of Iceland the Icelandic Instrument Fund, the Icelandic Science and Technology Research Program for Postgenomic Biomedicine, Nanoscience and Nanoscience and Nanotechnology, and the Taiwan National Science Council under the grant number NSC97-2112-M-239-003-MY3.

-
- * Electronic address: omarv@raunvis.hi.is
 † Electronic address: cstang@nuu.edu.tw
 ‡ Electronic address: vidar@raunvis.hi.is
- ¹ S. Datta, *Electronic Transport in Mesoscopic Systems* (Cambridge University Press, Cambridge, 1995).
 - ² Y. Imry, *Introduction to Mesoscopic Physics* (Oxford University Press, Oxford, 2001).
 - ³ J. P. Bird, R. Akis, D. K. Ferry, D. Vasileska, J. Cooper, Y. Aoyagi, and T. Sugano, Phys. Rev. Lett. **82**, 4691 (1999).
 - ⁴ A. P. S. de Moura, Y.-C. Lai, R. Akis, J. P. Bird, and D. K. Ferry, Phys. Rev. Lett. **88**, 6804 (2002).
 - ⁵ C. S. Tang, Y. H. Tan, and C. S. Chu, Phys. Rev. B **67**, 205324 (2003).
 - ⁶ M. Mendoza and P. A. Schulz, Phys. Rev. B **74**, 035304 (2006).
 - ⁷ C. S. Tang, W. W. Yu, and V. Gudmundsson, Phys. Rev. B **72**, 195331 (2005).
 - ⁸ O. Olendski and L. Mikhailovska, Phys. Rev. B **67**, 035310 (2003).
 - ⁹ G. Thorgilsson, C.-S. Tang, and V. Gudmundsson, Phys. Rev. B **76**, 195314 (2007).
 - ¹⁰ C. Muller, L. Worschech, and A. Forchel, Electron. Lett. **43**, 1392 (2007).
 - ¹¹ K. Kang, S. Y. Cho, J. J. Kim, and S. C. Shin, Phys. Rev. B **63**, 113304 (2001).
 - ¹² R. Franco, M. S. Figueira, and E. V. Anda, Phys. Rev. B **67**, 155301 (2003).
 - ¹³ K. Kobayashi, H. Aikawa, A. Sano, S. Katsumoto, and Y. Iye, Phys. Rev. B **70**, 035319 (2004).
 - ¹⁴ M. Sato, H. Aikawa, K. Kobayashi, S. Katsumoto, and Y. Iye, Phys. Rev. Lett. **95**, 066801 (2005).
 - ¹⁵ W. Lee, J. U. Kim, and H. Sim, Phys. Rev. B **77**, 033305 (2008).
 - ¹⁶ G. Kirzenow, A. S. Sachrajda, Y. Feng, R. P. Taylor, L. Henning, J. Wang, P. Zawadzki, and P. T. Coleridge, Phys. Rev. Lett. **72**, 2069 (1994).
 - ¹⁷ I. V. Zozoulenko, F. A. Maa, and E. H. Hauge, Phys. Rev. B **53**, 7987 (1996).
 - ¹⁸ M. Merlo, A. Braggio, N. Magnoli, and M. Sassetti, Phys. Rev. B **75**, 195332 (2007).
 - ¹⁹ S. A. Gurvitz, Phys. Rev. B **57**, 6602 (1998).
 - ²⁰ J. W. Park, K. S. Park, B. T. Lee, C. H. Lee, S. D. Lee, J. B. Choi, K.-H. Yoo, J. Kim, S. C. Oh, S. I. Park, et al., Appl. Phys. Lett. **75**, 566 (1999).
 - ²¹ K. Chang and F. M. Peeters, Phys. Rev. B **68**, 205320 (2003).
 - ²² C.-S. Tang and V. Gudmundsson, Phys. Rev. B **74**, 195323 (2006).
 - ²³ D. Huang, S. K. Lyo, K. J. Thomas, and M. Pepper, Phys. Rev. B **77**, 085320 (2008).
 - ²⁴ C. S. Tang and C. S. Chu, Phys. Rev. B **53**, 4838 (1996).
 - ²⁵ J. H. Bardarson, I. Magnusdottir, G. Gudmundsdottir, C. S. Tang, A. Manolescu, and V. Gudmundsson, Phys. Rev. B **70**, 245308 (2004).
 - ²⁶ V. Gudmundsson, C.-S. Tang, and A. Manolescu, Phys. Rev. B **72**, 153306 (2005).
 - ²⁷ G. Ordenez, K. Na, and S. Kim, Phys. Rev. A **73**, 022113 (2006).
 - ²⁸ C. S. Tang and C. S. Chu, Phys. Rev. B **60**, 1830 (1999).
 - ²⁹ D. Frustaglia, M. Hentschel, and K. Richter, Phys. Rev. Lett. **87**, 256602 (2001).
 - ³⁰ D. Frustaglia, M. Hentschel, and K. Richter, Phys. Rev. B **69**, 155327 (2004).
 - ³¹ Y.-T. Cui, J. C. Sankey, C. Wang, K. V. Thadani, Z.-P. Li, R. A. Buhrman, and D. C. Ralph, Phys. Rev. B **77**, 214440 (2008).
 - ³² M. Sigrist, T. Ihn, K. Ensslin, M. Reinwald, and W. Wegscheider, Phys. Rev. Lett. **98**, 036805 (2007).
 - ³³ V. I. Puller and Y. Meir, Phys. Rev. B **77**, 165421 (2008).

- ³⁴ J. Peng, B. Wang, and D. Y. Xing, Phys. Rev. B **71**, 214523 (2005).
- ³⁵ P. W. Anderson, Phys. Rev. **124**, 41 (1961).
- ³⁶ Z. Ma, J. Shi, and X. C. Xie, Phys. Rev. B **62**, 15352 (2000).
- ³⁷ S. Costamagna and J. A. Riera, Phys. Rev. B **77**, 235103 (2008).
- ³⁸ I. Weymann, Phys. Rev. B **78**, 045310 (2008).
- ³⁹ G. Cattapan and E. Maglione, Am. J. Phys. **71**, 903 (2003).
- ⁴⁰ M. Di Ventura and N. D. Lang, Phys. Rev. B **65**, 045402 (2002).
- ⁴¹ R. Landauer, IBM J. Res. Dev. **1**, 233 (1957).
- ⁴² M. Büttiker, Y. Imry, and R. Landauer, Phys. Rev. Lett. **96A**, 365 (1983).
- ⁴³ Y. Imry and R. Landauer, Rev. Mod. Phys. **71**, S306 (1999).
- ⁴⁴ M. Abramowitz and I. A. Stegun, *Handbook of Mathematical Functions - with Formulas, Graphs, and Mathematical Tables* (Dover Publications, Inc., 1965).
- ⁴⁵ A. V. Malyshev, P. A. Orellana, and F. Domnguez-Adame, Phys. Rev. B **74**, 033308 (2006).
- ⁴⁶ R. Žitko and J. Bonca, Phys. Rev. B **73**, 035332 (2006).
- ⁴⁷ U. Fano, Phys. Rev. **124**, 1866 (1961).
- ⁴⁸ L. P. Kouwenhoven, T. H. Oosterkamp, M. W. S. Danoe-sastro, M. Eto, D. G. Austing, T. Honda, and S. Tarucha, Science **278**, 1788 (1997).
- ⁴⁹ A. Wallraff, D. I. Schuster, A. Blais, L. Frunzio, R.-S. Huang, J. Majer, S. Kumar, S. M. Girvin, and R. J. Schoelkopf, Nature (London) **431**, 162 (2004).
- ⁵⁰ J. von Neumann and E. Wigner, Phys. Z. **30**, 465 (1929).
- ⁵¹ F. H. Stillinger and D. R. Herrick, Phys. Rev. A **11**, 446 (1975).
- ⁵² H. Friedrich and D. Wintgen, Phys. Rev. A **32**, 3231 (1985).
- ⁵³ S. Fan, P. Villeneuve, J. D. Joannopoulos, and H. A. Haus, Phys. Rev. Lett. **80**, 960 (1998).
- ⁵⁴ M. L. Ladrón de Guevara, F. Claro, and P. A. Orellana, Phys. Rev. B **67**, 195335 (2003).
- ⁵⁵ A. F. Sadreev, E. N. Bulgakov, and I. Rotter, Phys. Rev. B **73**, 235342 (2006).
- ⁵⁶ O. Olendski and L. Mikhailovska, Phys. Rev. B **66**, 35331 (2002).
- ⁵⁷ L. S. Cederbaum, R. S. Friedman, V. M. Ryaboy, and N. Moiseyev, Phys. Rev. Lett. **90**, 013001 (2003).
- ⁵⁸ F. Capasso, C. Sirtori, J. Faist, D. L. Sivco, S. N. G. Chu, and A. Y. Cho, Nature (London) **358**, 565 (1992).
- ⁵⁹ H. X. He, X. L. Li, N. J. Tao, L. A. Nagahara, I. Amlani, and R. Tsui, Phys. Rev. B **68**, 045302 (2003).
- ⁶⁰ J. Taylor, M. Brandbyge, and K. Stokbro, Phys. Rev. B **68**, 121101 (2003).